J Supercond Nov Magn (2014) 27:411–420
DOI 10.1007/s10948-013-2276-3

ORIGINAL PAPER

Synthesis and Properties Investigation of Non-equivalent Substituted W-Type Hexaferrite

Fengying Guo · Xiaomin Wu · Guijuan Ji · Jijing Xu · Lianchun Zou · Shucai Gan

Received: 10 April 2013 / Accepted: 27 May 2013 / Published online: 16 June 2013

Abstract A novel composed W-type hexaferrite $Ba_{1-x}La_xCo_2Fe_{16}O_{27}$ was rapidly synthesized via a sol–gel self-combustion reaction. The effects of lanthanum ions on the oxidation state of iron ions and cobalt ions in hexaferrite were explored by X-ray photoelectron spectroscopy. The changes of the Fe 2p X-ray absorption spectra indicated that the nonequivalent substitution can lead to the transition $Fe^{3+} \rightarrow Fe^{2+}$ in $Ba_{1-x}La_xCo_2Fe_{16}O_{27}$. However, the oxidation state of cobalt ions was maintained as Co^{2+}. Moreover, the effects of La content on the phase composition, structural parameters, morphology, and static magnetic properties were also investigated in detail by using the X-ray diffractometer, scanning electron microscope, and vibrating sample magnetometer. The results indicated that the structural parameters decreased regularly with increasing the La content, and the magnetic properties were enhanced after substitution, which is beneficial for their application in various electrical devices employed for industrial and military applications.

Keywords La substituted · Sol–gel self-combustion · X-ray photoelectron spectroscopy · Microstructure · W-Hexaferrite

The authors declare that they have no conflict of interest.

F. Guo · X. Wu · G. Ji · L. Zou (✉) · S. Gan
College of Chemistry, Jilin University, Changchun 130026, China
e-mail: zoulianchun@126.com

S. Gan (✉)
e-mail: gansc@jlu.edu.cn

J. Xu
State Key Laboratory of Rare Earth Resource Utilization, Changchun Institute of Applied Chemistry Chinese Academy of Sciences, Changchun 130022, China

1 Introduction

W-type hexaferrites were an important soft magnetic material in the field of electronic and automatic devices, especially in the application field of microwave absorbing agents, based on their fascinating magnetic and electromagnetic properties. Rare-earth elements have been doped into ferrites due to their typical magneto-crystalline anisotropy and high coercivity, which may affect the electromagnetic properties of ferrite magically [1–3]. Therefore, many methods for the synthesis of rare-earth doped hexaferrite have been intensively developed. However, the classical ceramic method for preparing W-type hexaferrite requires a high calcination temperature (usually about 1300–1400 °C) to cause the solid reaction, which often results in the formation of coarse aggregate, and the resulting particle's magnetic properties easily decreased due to the large particle size [4]. Impurity phases will accompany with target ferrites when using flux to decrease the sintering temperature [5, 6]. The chemical coprecipitation method has the same problem of impurity phases as the method of using flux [7]. László Trif [8] has synthesized nickel-zinc doped W-type hexaferrite using the sol–gel self-combustion method at a low temperature of 1200 °C, however, the sintering time was up to 4 h. Hence, low calcination temperature and short calcination time were still the significant direction of research in synthetic methods of hexaferrites. Furthermore, it is well known that the Fe $2p_{3/2}$ component with the binding energy of 710.8–711.0 eV was assigned to the Fe^{3+} state while that with 709.5–710.0 eV, to the Fe^{2+} state [9]. A number of works have been made to investigate the oxidation state of iron in various compounds based on the shape of Fe 2p X-ray photoelectron spectra. Marina V. Bukhtiyarova [10] has prepared Sr-hexaferrites $SrMn_xFe_{12-x}O_{19}$ and confirmed that the main components on the surface are in oxidized

states: Mn^{3+} and Fe^{3+} based on XPS data. A.T. Kozakov [9] has measured the Fe 2p, Fe 3p, and Fe 3s X-ray photoelectron spectra to determine the Fe^{3+}/Fe^{2+} ratio in the $BaFe_{1/2}Nb_{1/2}O_3$ sample. One of the problems which has not yet been resolved was the question of whether rare-earth substituted W-type hexaferrites contain not only Fe^{3+}, but also Fe^{2+} ions.

Therefore, in the present work, systematically research and analysis on the synthesis, microstructure, magnetic properties, and charge equilibrium problem were taken on the W-type hexaferrite $Ba_{1-x}La_xCo_2Fe_{16}O_{27}$. The materials are synthesized by the modified sol–gel self-combustion method and the synthesized temperature and time dramatically decreased, which reduced energy consumption effectively. Due to the substitution of rare-earth element La, the microstructure and magnetic properties were improved, which are beneficial for their application in various electrical devices employed for industrial and military applications. Furthermore, the confused problem of charge equilibrium in the nonequivalent substitution process has been explained rationally via analyzing the X-ray photoelectron spectroscopy of iron and cobalt ions.

2 Experimental Section

2.1 Powder Preparation

Rare-earth doped W-type hexaferrite $Ba_{1-x}La_xCo_2Fe_{16}O_{27}$ powders with $x = 0$, 0.05, 0.10, 0.15, and 0.20 were synthesized by the sol–gel self-combustion method. The raw materials in this work, such as $Fe(NO_3)_3{\cdot}9H_2O$ (Aladdin, ≥98.5 %), $Ba(NO_3)_2$ (Aladdin, ≥99.0 %), $Co(NO_3)_2{\cdot}6H_2O$ (Aladdin, ≥99.0 %), $La(NO_3)_3{\cdot}6H_2O$ (Aladdin, ≥98.0 %), and citric acid monohydrate (Aladdin, ≥99.5 %) were used as received without further purification. The synthetic process can be described as follows: The stoichiometric amounts of barium, ferric, lanthanum, and cobalt nitrate were dissolved together in distilled water, stirring until they were completely dissolved to form a transparent mixture solution. The citric acid was added into the mixture solution to form a homogeneous transparent solution. The molar ratio of citric acid to metals equal to 2. Then the ammonia was added dropwise to the solution to adjust the pH value to 7.0. After continuous stirring for 6 h at room temperature, the solution was evaporated at 80 °C until a transparent sol was obtained, and then the resulting sol was heated at 110 °C for 24 h in an oven to get the dried gel. The dried gel ignited by a little amount of ethanol and burned in a self-propagation combustion manner to form a dark-gray loose powder. The as-burned powders were calcined at various temperatures (1100 °C, 1150 °C, 1200 °C, 1250 °C, and 1300 °C) for 3 h and also calcined for various times (1 h, 2 h, 3 h, 4 h, and 5 h) at 1200 °C in air atmosphere in a muffle furnace.

2.2 Characterization

The thermal decomposition behavior of the dried gel was examined by means of thermogravimetry (TG) and differential scanning calorimetry (DSC) with a heating rate of 10 °C/min under synthetic air atmosphere (80 % N_2, 20 % O_2) flow of 60 mL/min on the TGA/DSC 1600 LF (METTLER TOLEDO, Switzerland). The phase identification was carried out using D/max 2500 PC (Rigaku, Japan) X-ray powder diffraction (XRD) with Cu Kα radiation ($\lambda = 1.54056$ Å). Fourier transform infrared spectra (FT-IR) were recorded on an IR-Affinity-1 (Rigaku, Japan) spectrophotometer from 400 to 4000 cm^{-1} by using the KBr disk method. The Scanning electron microscope (SEM) examination of the synthesized hexaferrite powders was performed using a XL 30ESEM (Philips, Netherlands) scanning electron microscope. The magnetic measurement for synthesized hexaferrite powders was taken on a MPMS SQUID VSM (Quantum Design, America) vibrating sample magnetometer (VSM) in the applied field from 0 to ±10000 Oe at room temperature. The X-ray photoelectron spectroscopy (XPS) was performed with an EscaLab 250Xi (Thermo Scientific, England) spectrometer using monochromatic Al Kα radiation.

3 Results and Discussion

3.1 Phase Analysis

Figure 1 shows the XRD patterns of powders calcined at 1100 °C, 1150 °C, 1200 °C, 1250 °C, and 1300 °C for 3 h in the air, respectively. The obtained powders do not have a W-type hexaferrite crystalline phase, which calcined at 1100 °C and 1150 °C. Four characteristic peaks for M-type ferrite $BaFe_{12}O_{19}$ ($2\theta = 30.307°$, 32.250°, 34.144°, and 37.134°) marked by their indices (1 1 0), (1 0 7), (1 1 4), and (2 0 3) are observed for samples. These peaks are consistent with the database in JCPDS file (JCPDS# 27-1029). However, a spinel ferrite $CoFe_2O_4$ (JCPDS# 22-1086) phase is also observed as an impurity, as indicated by the reflections mainly at $2\theta = 35.539°$, 43.264°, 56.544°, and 62.674°. When raising the calcination temperature to 1200 °C, the XRD pattern of powder shows a pure crystalline phase of W-type hexaferrite $Ba_{1-x}La_xCo_2Fe_{16}O_{27}$ according to the standard card of JCPDS# 78-0135, and the characteristic peaks at $2\theta = 30.307°$, 32.375°, 34.468°, and 62.973° are correspondent with (1 1 0), (1 0 10), (1 1 6), and (2 2 0) crystal indices, respectively. Furthermore, no impurity phases are observed. The powders calcined at 1250 °C and 1300 °C show identical pure phase of W-type hexaferrite. The XRD results indicate that when the calcination temperature is lower than 1200 °C, the main phases in powders are the mixture

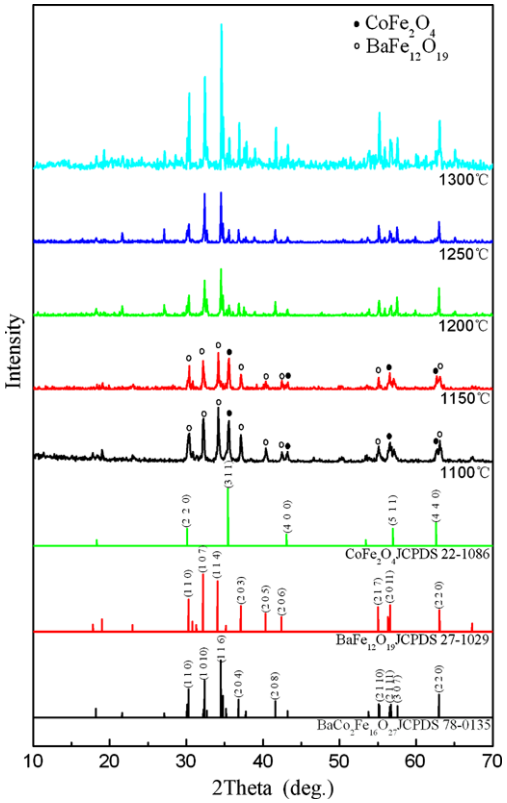

Fig. 1 XRD patterns of powders calcined at different temperatures for 3 h

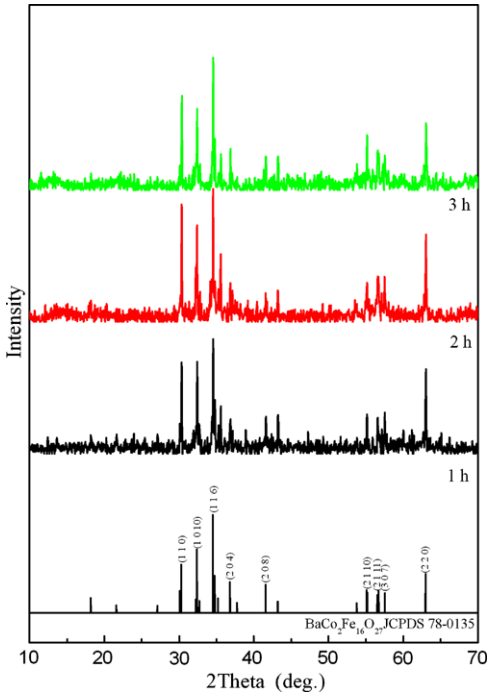

Fig. 2 XRD patterns of powders calcined at 1200 °C for different times

of $BaFe_{12}O_{19}$ and $CoFe_2O_4$. Pure W-type phase can be obtained at a relative low calcination temperature of 1200 °C by using the sol–gel self-combustion method, which lowers 100 °C than using the traditional solid-state reaction method. This method has obvious advantages in reducing the calcination time and saving the energy effectively.

XRD patterns of powders calcined at 1200 °C for 1 h, 2 h, and 3 h, respectively, are provided in Fig. 2. As shown in the figure, the powder calcined for 1 h presents a pure phase of W-type hexaferrite. The diffraction peaks at $2\theta = 30.307°$, 32.375°, 34.568°, and 63.023° are the characteristic peaks for W-type hexaferrite $BaCo_2Fe_{16}O_{27}$ (JCPDS# 78-0135), and the corresponding crystal indices are (1 1 0), (1 0 10), (1 1 6), and (2 2 0). Impurity peaks are not detected in the powder calcined for 1 h. When extending the calcination time to 2 h and 3 h, the position and relative intensity of all diffraction peaks match well with the standard powder diffraction data (JCPDS# 78-0135), which indicates that the synthesized powders all have pure crystalline phase of W-type hexaferrite. The results of XRD patterns illustrate that the pure W-type crystalline phase of $Ba_{1-x}La_xCo_2Fe_{16}O_{27}$ could be easily synthesized in a shorter calcination time of 1 h at a relatively low calcination temperature of 1200 °C by using sol–gel self-combustion method. The investigation suggests that the as-burnt powders obtained by sol–gel self-combustion method have an excellent sintering activity, which can rapidly develop into pure W-type hexaferrite at low calcination temperature. The sol–gel self-combustion method effectively shortens the calcination time and reduces the energy losses under our experimental conditions. The calcination time of pure W-type hexaferrite used in our study is much lower than that of László Trif et al., who synthesized nickel-zinc doped W-type hexaferrite using sol–gel self-combustion method at 1200 °C for 4 h.

XRD patterns of $Ba_{1-x}La_xCo_2Fe_{16}O_{27}$ (where $x = 0.00$, 0.05, 0.10, 0.15, 0.20, and 0.25) powders calcined at 1200 °C for 1 h are shown in Fig. 3. In the case of $x \leq 0.20$, the characteristic (1 1 0), (1 0 10), (1 1 6), and (2 2 0) reflections of W-type hexaferrite phase (identified by JCPDS# 78-0135) are clearly observed, and no XRD patterns arising from other phase appear. It confirms that the as-synthesized products are of high purity and good crystallinity. However, the impurity phase of La_2O_3 is observed at $2\theta = 31.40°$ and 53.75° (identified by JCPDS# 22-0369) when $x = 0.25$. Meanwhile, the crystalline phase of powder become a mixture of $BaFe_{12}O_{19}$ (JCPDS# 43-0002) and a small amount of $CoFe_2O_4$ (identified by JCPDS# 22-1086). It is well known that the ionic radius of Ba^{2+} and La^{3+} is 1.380 Å and 1.032 Å, respectively [11]. La^{3+} ions can replace the Ba^{2+} ions and enter into the W-type hexaferrite crystal lattices when the La content is small. With the increasing of La content, the lattice distortion of W-type hexaferrite increased due to the difference of ionic radius between Ba^{2+} ions and La^{3+} ions [12]. The serious lattice distortion will

cause Fe^{3+} ions not to fix at original lattice site and to be squeezed out of the crystal lattice to form impurity phase of $CoFe_2O_4$. And the redundant La^{3+} ions will aggregate on the grain boundaries forming La_2O_3 phase. Therefore, the maximum substitution amount of La^{3+} ions cannot overpass 0.2 under our experiment conditions.

3.2 Thermal Analysis

Figure 4 provides the thermal decomposition behavior of dried gel powder at temperatures ranging from 50 to 900 °C under the atmosphere of air. The TG curve exhibits three weight loss steps corresponding to one sharp exothermic peak and three small endothermic peaks in the DSC curve. The first step occurs at the temperature ranging from 60 to 120 °C with the weight loss of 3.7 %, which corresponds to the endothermic peak in DSC curve. This weight loss can be ascribed to the evaporation of planar and inner water in the dried gel. The second step in the TG curve shows a drastic weight loss about 69.8 %, which is accompanied with the largest sharp exothermic peak around 204 °C in the DSC curve. This is associated with the autocatalytic oxidation–reduction reaction between the citric acid and metal nitrates with the liberation of H_2O, CO_2, and N_2O. The third step occurs at the temperature ranging from 570 to 620 °C with the weight loss of 14.2 % attributed to the decomposition of the remaining citric acid accompanied by the two border endothermic peaks at 587 and 616 °C in the DSC curve.

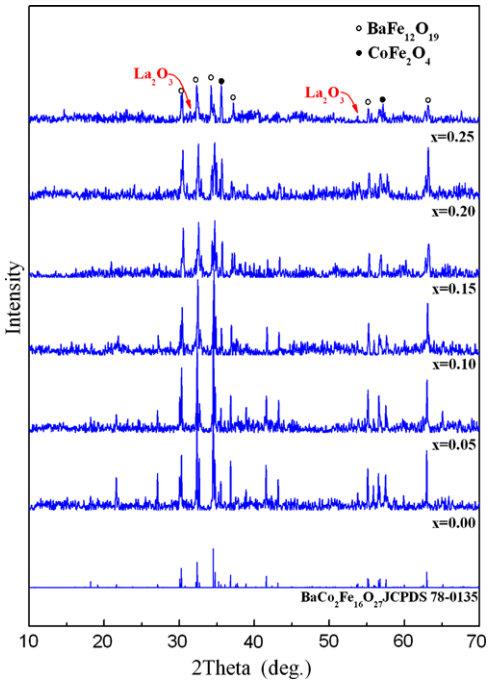

Fig. 3 XRD patterns of powders with different La content *x*

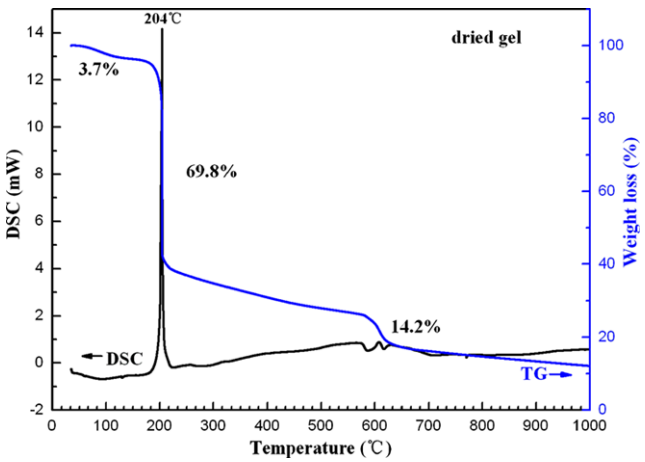

Fig. 4 TG/DSC curve of dried gel powder

3.3 FT-IR Spectra

Figure 5 illustrates FT-IR spectra of the dried gel, as-burned powder and powder calcined at 1200 °C. The spectrum of dried gel shows the characteristic bands of O–H stretching vibration of citric acid at 2700–3700 cm^{-1}, asymmetrical vibration of $–CO_2$ at 1600 cm^{-1} and the N–O stretching vibration of NO_3^- at 1380 cm^{-1}, respectively. In the as-burned powder spectrum, the characteristic absorption bands corresponding to O–H, $–CO_2$, and N–O weaken drastically, which suggests that the NO_3^- and $–CO_2$ groups participate in the self-combustion reaction. This is in good agreement with the results of TG–DSC curve. The absorption bands at 583 cm^{-1} and 425 cm^{-1}, shown in as-burnt powder and calcined powder spectra, can be ascribed to the metal-oxygen stretching vibration at the tetrahedral and octahe-

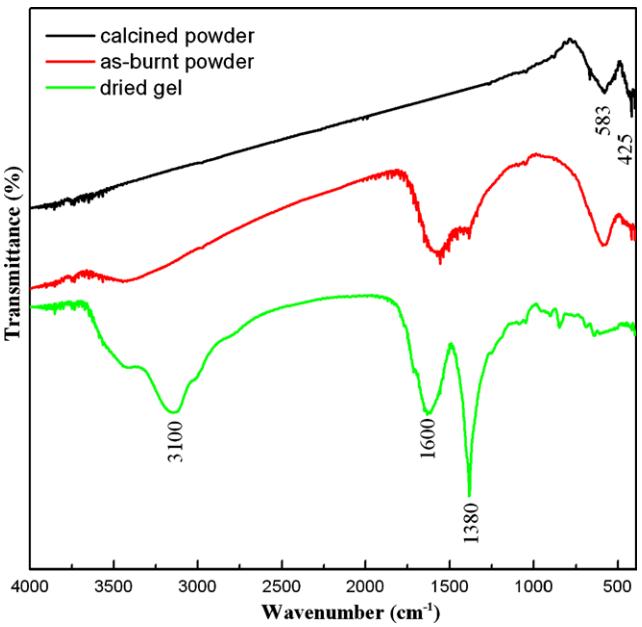

Fig. 5 FT-IR spectra of the dried gel, as-burnt and calcined powder

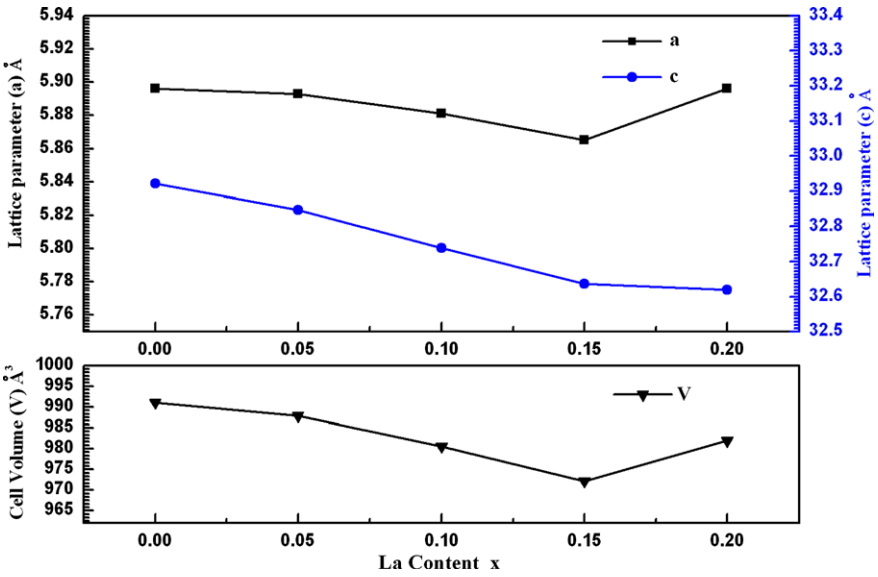

Fig. 6 Variation of lattice parameters (a and c) and cell volume V with different La^{3+} content x

dral sites, respectively. The characteristic absorption bands corresponding to the NO_3^- and $-CO_2$ finally disappear in the powder calcined at 1200 °C. From the FT-IR spectra and TG-DSC curve results of samples, we suggest that the oxidation–reduction reaction take place between metal nitrate and citric acid in the self-combustion process. A quantity of energies generated from the reaction support the self-combustion to the end completely. The crystalline phases of metal oxides appear after the self-combustion reaction.

3.4 Microstructure Parameters and Morphology

The dependence of lattice parameters (a and c) and cell volume (V) on La substitution content x are provided in Fig. 6. The lattice parameters of samples are computed using the "d" value and their respective (hkl) parameters by computer software Jade 5.0 and the corresponding values are given in Table 1. The results suggest that the lattice parameters (a and c) and cell volume (V) all decrease regularly with increasing of La content x. As shown in Table 1, the lattice parameter a decreases from 5.896 Å ($x = 0.00$) to 5.865 Å ($x = 0.15$), while the lattice parameter c decreases from 32.921 Å ($x = 0.00$) to 32.619 Å ($x = 0.20$). The decrease in the lattice parameters with the increase of La content is expected to be due to the smaller ionic radius of La^{3+} (1.032 Å) compared to that of Ba^{2+} (1.38 Å) [13, 14]. It is well known that the crystal structure of W-type hexaferrite can be considered as a superposition of R and S blocks along the hexagonal c-axis with a structure of RSSR*S*S*, where R is a three-oxygen-layer block with composition $BaFe_6O_{11}$, S (Spinel block) is a two-oxygen-layer block with composition Fe_6O_8 and asterisk means that the respective block turns 180° around the hexagonal axis. One Ba^{2+} ion is found in the R block replacing oxygen [15]. La^{3+} ions are expected to enter into the R block in place of Ba^{2+} ions, which results in a shrink in crystal cell along c-axis and a-axis due to the difference in ionic radius between Ba^{2+} and La^{3+}. Consequently, the value of lattice parameters (a and c) decrease with increasing La^{3+} content. In addition, the cell volume of powders, which was calculated by the equation of $V = 0.866a^2c$, decreases from 991.07 $Å^3$ ($x = 0.00$) to 972.19 $Å^3$ ($x = 0.15$). However, the upturn of lattice parameter a and cell volume V for the $x = 0.2$ sample can be attributed to the serious lattice distortion which was due to the increasing of La content. Accordingly, we may suggest that the replacement of Ba^{2+} by La^{3+} ions has important influences on microstructure parameters in W-type hexaferrite. La substitution can decrease the lattice parameters (a and c) and cell volume (V) of W-type hexaferrite. From Table 1, it can be seen that with the increasing La content x, the porosity of the samples increases from 0.22 to 0.27 which was calculated based on the equation of $P = 1 - d_B/d_x$. This increase can be explained as follows: the La^{3+} ion radius is smaller than that of Ba^{2+} ion, most La^{3+} ions go into the hexagonal crystal structure, then the porosity increases based on the difference between the Fe^{3+} (0.64 Å) and Fe^{2+} (0.76 Å) radii as well as on the difference in the ionic radii of La^{3+} (1.032 Å) and Ba^{2+} (1.38 Å) [16].

The SEM images of unsubstituted hexaferrite and La substituted hexaferrite powders are provided in Figs. 7(a) and 7(b), respectively. It can be clearly noted that the particles are homogeneous and present a well-defined hexagonal flake shape. Figure 7(a) shows the average particle size is approximately 6–7 μm, while the La substituted hexaferrite powders exhibit a smaller particle size about 2.5–3 μm as shown in Fig. 7(b). Crystallite size is found to decrease in La substituted powders. Segregation of La^{3+} ions on or

Table 1 The values of different parameters calculated for samples with different La^{3+} content

La content x	0.00	0.05	0.10	0.15	0.20
Lattice parameter (a (Å)) ±0.001	5.896	5.893	5.881	5.865	5.896
Lattice parameter (c (Å)) ±0.001	32.921	32.847	32.738	32.636	32.619
Cell volume (V (A^3))	991.07	987.84	980.56	972.19	981.98
Bulk density (d_{Bulk}/g cm^{-3}) ±0.01	4.11	3.96	3.93	3.84	3.91
X-Ray density ($d_{X\text{-}ray}$/g cm^{-3}) ±0.01	5.30	5.32	5.36	5.40	5.35
Porosity (P/%)	0.22	0.26	0.27	0.29	0.27
Saturation magnetization (M_s (emu g^{-1}))	71.18	74.17	75.76	74.83	72.77
Remanent magnetization (M_r (emu g^{-1}))	8.29	8.09	6.87	11.36	12.64
Coercivity (H_c (Oe))	151.48	120.14	88.81	137.48	193.27

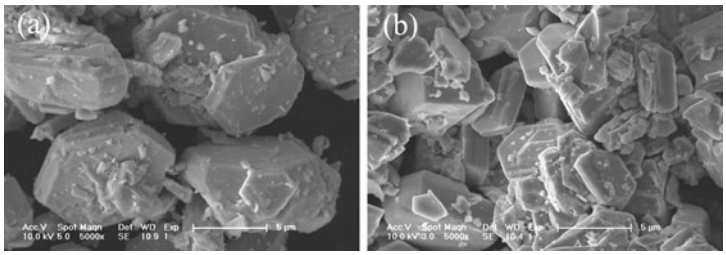

Fig. 7 The SEM images of $BaCo_2Fe_{16}O_{27}$ and $Ba_{0.85}La_{0.15}Co_2Fe_{16}O_{27}$ samples

near the grain boundaries, which impedes the grain boundary mobility, may be the reason for this decrease [17]. The investigation illustrates that La substitution can decrease the particle size of ferrite effectively in hexaferrite in our experiment condition. Consequently, the improvements of lattice parameter and particle size are beneficial for their application in various electrical devices employed for industrial and military applications.

3.5 XPS Investigations

To assess the oxidation states of cobalt and iron on the surface of the hexaferrites, samples were submitted to Co 2p and Fe 2p spectra investigation of X-ray photoelectron spectroscopy (XPS). Survey spectra obtained from $BaCo_2Fe_{16}O_{27}$ and $Ba_{0.85}La_{0.15}Co_2Fe_{16}O_{27}$ samples are presented in Fig. 8. The binding energies obtained in the XPS analysis were corrected for specimen charging by referencing the C 1s line to 284.8 eV. The corresponding electron binding energies of Fe 2p and Co 2p photoelectron peaks are shown in Table 2. XPS survey spectra reveal strong signals from Fe, Co, Ba, C, and O. The relative La content in $Ba_{0.85}La_{0.15}Co_2Fe_{16}O_{27}$ sample is so small that La 4d peak is not marked due to the weak signal strength.

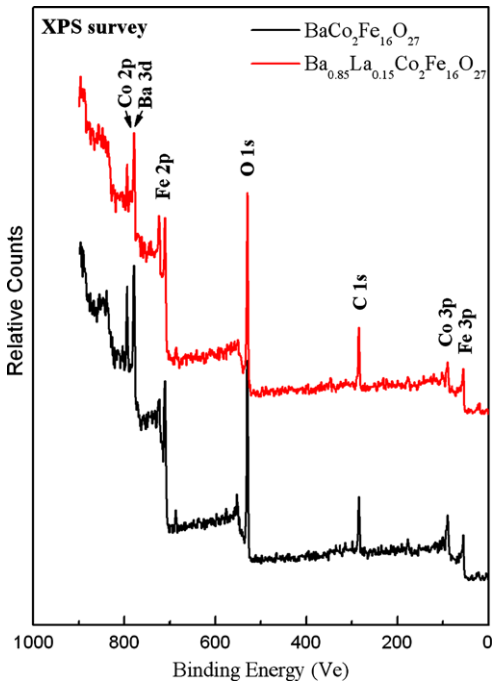

Fig. 8 The XPS survey spectra of $BaCo_2Fe_{16}O_{27}$ and $Ba_{0.85}La_{0.15}Co_2Fe_{16}O_{27}$ samples

Figure 9 displays the high-resolution XPS spectra of Co 2p in hexaferrites $BaCo_2Fe_{16}O_{27}$ and $Ba_{0.85}La_{0.15}Co_2Fe_{16}O_{27}$. The Co 2p binding energy of $BaCo_2Fe_{16}O_{27}$ sample is 779.5 and 794.8 eV, as shown in Fig. 9, which are assigned to Co $2p_{3/2}$ and Co $2p_{1/2}$, respectively. The spectrum of the $Ba_{0.85}La_{0.15}Co_2Fe_{16}O_{27}$ sample is similar to that of the $BaCo_2Fe_{16}O_{27}$ sample. The binding energy of Co $2p_{3/2}$ and Co $2p_{1/2}$ in $Ba_{0.85}La_{0.15}Co_2Fe_{16}O_{27}$ sample is

Table 2 The Fe 2p and Co 2p binding energy of samples

Sample	Binding energy (eV)			
	Fe $2p_{3/2}$	Fe $2p_{1/2}$	Co $2p_{3/2}$	Co $2p_{1/2}$
$BaCo_2Fe_{16}O_{27}$ (Exp.)	711.3	724.4	779.5	794.8
$Ba_{0.85}La_{0.15}Co_2Fe_{16}O_{27}$ (Exp.)	710.7	724.5	779.4	794.3
Fe_2O_3 (Ref.)	711.6	724.9	–	–
Fe_3O_4 (Ref.)	710.8	724.6	–	–
CoO (Ref.)	–	–	779.6	794.5

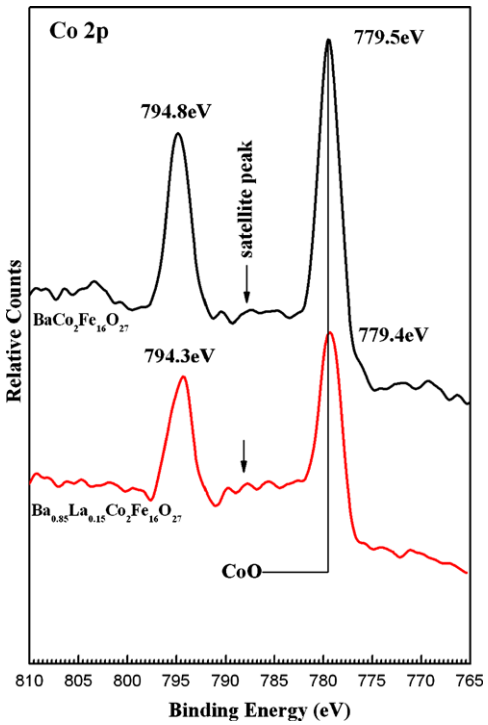

Fig. 9 The Co 2p XPS spectra of $BaCo_2Fe_{16}O_{27}$ and $Ba_{0.85}La_{0.15}Co_2Fe_{16}O_{27}$ samples

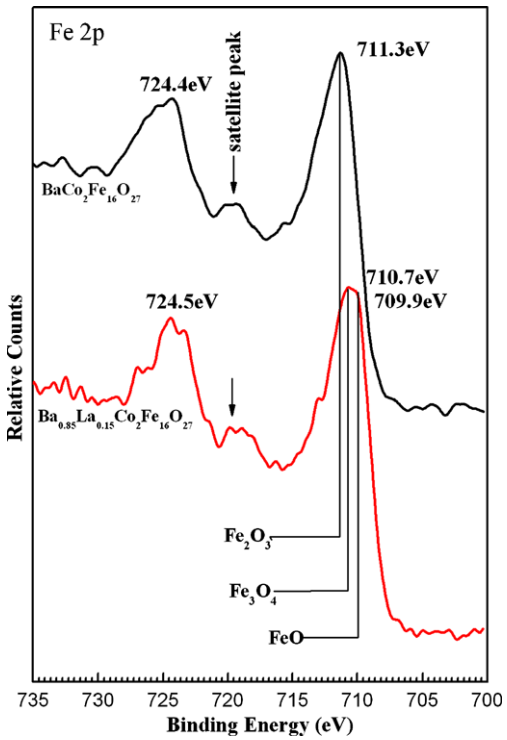

Fig. 10 The Fe 2p XPS spectra of $BaCo_2Fe_{16}O_{27}$ and $Ba_{0.85}La_{0.15}Co_2Fe_{16}O_{27}$ samples

around 779.4 and 794.3 eV, respectively. Satellite peaks are observed at higher binding energy beside the Co $2p_{3/2}$ peak in the spectra of the two samples, which are the characteristics of paramagnetic Co(II) high-spin complexes. The general line shape of the Co 2p spectrum and the position of the Co $2p_{3/2}$ and Co $2p_{1/2}$ are all in close agreement with data reported by F. Bensebaa et al. for pure CoO crystals in which the Co $2p_{3/2}$ and Co $2p_{1/2}$ peak lies in 779.6 and 794.5 eV, respectively [18]. Consequently, it can be presumed from the Co 2p XPS spectra results that the oxidation state of cobalt in $BaCo_2Fe_{16}O_{27}$ and $Ba_{0.85}La_{0.15}Co_2Fe_{16}O_{27}$ is in form of Co^{2+}, which confirms that the cobalt ions do not participate in charge transfer reactions during the nonequivalent substitution process.

The Fe 2p XPS spectra of $BaCo_2Fe_{16}O_{27}$ and $Ba_{0.85}La_{0.15}Co_2Fe_{16}O_{27}$ powder surface are shown in Fig. 10. For the unsubstituted sample $BaCo_2Fe_{16}O_{27}$, the binding energy of Fe $2p_{3/2}$ and $2p_{1/2}$ is 711.3 and 724.4 eV, respectively. The binding energy is comparable to that of corresponding photoelectrons of Fe 2p in Fe_2O_3 according to S. William et al., who reported the binding energy was 711.6 and 724.9 eV for Fe $2p_{3/2}$ and Fe $2p_{1/2}$ in Fe_2O_3, respectively [19]. The spectrum contains an intense satellite peak at binding energy about 718.9 eV for $BaCo_2Fe_{16}O_{27}$, which is observed to be characteristic for Fe^{3+} according to the reported literatures [20, 21]. Hence, it can be speculated that the oxidation state of Fe existing in unsubstituted sample $BaCo_2Fe_{16}O_{27}$ is Fe^{3+}. The XPS spectrum of $Ba_{0.85}La_{0.15}Co_2Fe_{16}O_{27}$ exhibits two strong peaks at 710.7 and 724.5 eV, attributed to Fe $2p_{3/2}$ and Fe $2p_{1/2}$, respectively. The XPS spectrum shape of $Ba_{0.85}La_{0.15}Co_2Fe_{16}O_{27}$ sample is similar to that of $BaCo_2Fe_{16}O_{27}$ sample, as shown in Fig. 10, however, the position of Fe $2p_{3/2}$ peak shifts

toward lower binding energy side and located at about 710.7 eV. This binding energy is comparable to that of corresponding photoelectrons of Fe $2p_{3/2}$ in Fe_3O_4 according to the results of S. William et al., who reported the binding energy was 710.8 eV [19]. Moreover, a shoulder peak at the position of 709.9 eV corresponding to Fe $2p_{3/2}$ in FeO can also be detected in XPS spectrum of $Ba_{0.85}La_{0.15}Co_2Fe_{16}O_{27}$. The intensity of the satellite peak of $Ba_{0.85}La_{0.15}Co_2Fe_{16}O_{27}$ became weaker compared with that of $BaCo_2Fe_{16}O_{27}$ as shown in Fig. 10. According to the binding energy of Fe $2p_{3/2}$, taking into account the satellite peak in the Fe 2p spectra, we suggest that the surface of the $Ba_{0.85}La_{0.15}Co_2Fe_{16}O_{27}$ sample is enriched by Fe^{3+}, accompanied by a large amount of Fe^{2+}. This means that the substitution of La^{3+} ions leads to the oxidation state change of Fe from Fe^{3+} to Fe^{2+} in hexaferrite. The variation of oxidation state of Fe indicated that the following charge transfer reaction occurred during the nonequivalent substitution process: $Ba^{2+} + Fe^{3+} \rightarrow La^{3+} + Fe^{2+}$. A parts of Fe^{3+} ions transfer into Fe^{2+} to balance the valence states, when trivalent La^{3+} ions replaced divalent Ba^{2+} ions in hexaferrite. The XPS investigations here make clear that the nonequivalent substitution has important effect on oxidation state of iron ions in hexaferrite. Based on the XPS results, the iron and cobalt are mainly in oxidized state of Fe^{3+} and Co^{2+}, respectively, in unsubstituted hexaferrite. However, it turned out to be Fe^{3+}/Fe^{2+} and Co^{2+}, respectively, in La substituted hexaferrite. According to the above investigations, the confused problem of charge equilibrium during the nonequivalent substitution process has been explained rationally.

3.6 Magnetic Properties

The influence of La substitution content on magnetic properties is also investigated by using vibrating sample magnetometer. Figure 11 shows the curves of magnetic hysteresis at room temperature for samples with different La content calcined at 1200 °C for 1 h. The corresponding values of coercivity H_c, saturation magnetization M_s and remanent magnetization M_r are given in Table 1. It is observed that the samples of La substituted hexaferrites exhibit higher saturation magnetization and lower coercivity than that of unsubstituted sample. As shown in Table 1, the saturation magnetization increases up to 75.76 emu g^{-1} ($x = 0.10$) and then decreases with the increasing of La content. On the one hand, the composition of ferrite is one of the important factors in saturation magnetization. Due to the substitution of Ba^{2+} by La^{3+}, the lattice parameters shrink as Fig. 6 indicates. Correspondingly, the distance of Fe–O decreases and the Fe^{3+}–O–Fe^{3+} superexchange interaction for 12k and 2b sublattice was enhanced [22]. Therefore, the saturation magnetization of La substituted hexaferrites is higher than that

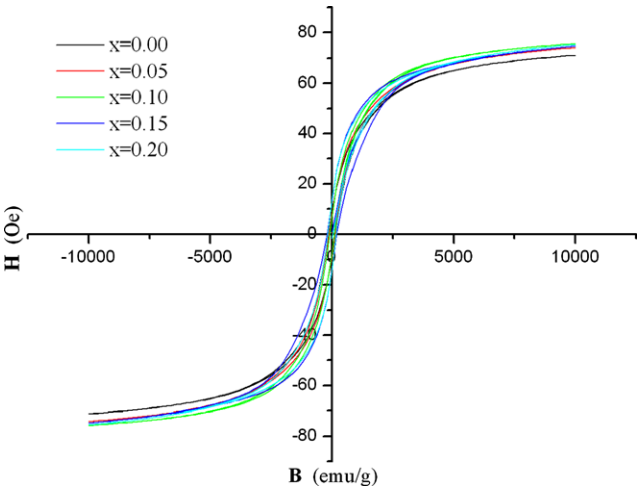

Fig. 11 Variation of magnetic properties (M_s and H_c) with different La^{3+} content x

of unsubstituted hexaferrite. On the other hand, the magnetic moment of each composition depends on the magnetic moments of ions involved. The magnetic moment of Fe^{3+} and Fe^{2+} are 5 μ_B and 4 μ_B, respectively. The saturation magnetization will decrease slightly after La content exceeding 0.15. The decreasing of M_s for $x = 0.15$ and 0.20 samples can be attributed to the appearance of abundance of Fe^{2+}, which decreases the net magnetic moment according to the chemical equation of $Ba^{2+} + Fe^{3+}(5\ \mu_B) \rightarrow Fe^{2+}(4\mu_B) + La^{3+}$ [23]. As a result, the value of M_s decreases slightly but still higher than that of unsubstituted sample, when La content exceeds 0.15. Above all, it can be identified from the results of magnetization measurements that La substitution can enhance the magnetic properties of W-type hexaferrite in our experiment conditions. Moreover, the coercivity of ferrite is affected combined by many factors such as shape anisotropy, magneto-crystalline anisotropy, and saturation magnetization [24]. The coercivity could be explained by the equation as follows [25]:

$$H_c = 2K/\mu_0 M_s$$

where K is the magneto-crystalline anisotropy constant, μ_0 is initial permeability, and M_s is the saturation magnetization. Here, the value of coercivity H_c is inversely proportional to that of saturation magnetization M_s according to the above equation, which is consistent with the results reported earlier [26]. Hence, the H_c decreases firstly and then increases with the increasing of La content. The results of coercivity indicate that the as-prepared samples are soft magnetic materials. The magnetic properties of the present La substituted hexaferrite particles with high saturation magnetization and low coercivity are favorable for their

applications such as in magnetic recording and microwave devices.

4 Conclusions

Rare-earth substituted W-type hexaferrites of $Ba_{1-x}La_xCo_2Fe_{16}O_{27}$ were synthesized by the sol–gel self-combustion method. This method provides a simple, fast, and low temperature synthesis process. With the improved sol–gel self-combustion method, the synthesized temperature and calcination time of pure W-type hexaferrites powders decreased from 1350 °C/4 h to 1200 °C/1 h compared with the normal solid state method, which reduced energy consumption effectively. Microstructure and magnetic properties investigation showed that lattice parameters and magnetization were strongly influenced by La content. With the increasing of La content, the crystal cell volume decreases from 991.07 to 972.19 Å^3 and the particle size also decreases from 6–7 to 2.5–3 μm. The saturation magnetization increases from 71.18 to 75.76 emu/g. The improvements of microstructure and magnetic properties are beneficial for their application in various electrical devices employed for industrial and military applications. Furthermore, XPS measurements were undertaken to understand the effect of nonequivalent substitution on oxidation states of iron and cobalt ions. The results revealed that the oxidation state of iron should be changed from Fe^{3+} to Fe^{2+}; however, the oxidation state of cobalt was Co^{2+}, which was consistently in the nonequivalent substitution process. Thus, the confused problem of charge equilibrium has been explained rationally.

Acknowledgements This present work was financially supported by the key technology and equipment of efficient utilization of oil shale resources, No. OSR-5, and the National Science and Technology Major Projects, No. 2008ZX05018-005.

References

1. Das, R., Jaiswal, A., Adyanthaya, S., Poddar, P.: Origin of magnetic anomalies below the Néel temperature in nanocrystalline $LuMnO_3$. J. Phys. Chem. C **114**, 12104–12109 (2010)
2. Søgaard, M., Hendriksen, P.V., Mogensen, M.: Oxygen nonstoichiometry and transport properties of strontium substituted lanthanum ferrite. J. Solid State Chem. **180**, 1489–1503 (2007)
3. Langhof, N., Göbbels, M.: Hexaferrites and phase relations in the iron-rich part of the system. J. Solid State Chem. **182**, 2725–2732 (2009)
4. Sharma, R., Agarwala, R.C., Agarwala, V.: A study on the heat-treatments of nanocrystalline nickel substituted BaW hexaferrite produced by low combustion synthesis method. J. Magn. Magn. Mater. **312**, 117–125 (2007)
5. Kračunovska, S., Töpfer, J.: Synthesis, sintering behavior and magnetic properties of Cu-substituted Co_2Z hexagonal ferrites. J. Mater. Sci., Mater. Electron. **22**, 467–473 (2011)
6. Collumb, A., Lambert-Andron, B., Boucherle, J.X., Samaras, D.: Crystal structure and cobalt location in the W-type hexagonal ferrite [Ba]Co_2-W. Phys. Status Solidi **96**, 385–395 (1986)
7. Wang, J., Zhang, H., Bai, S.X., Chen, K., Zhang, C.G.: Microwave absorbing properties of rare-earth elements substituted W-type barium ferrite. J. Magn. Magn. Mater. **312**, 310–313 (2007)
8. Trif, L., Tolnai, G., Sajó, I., Kálmán, E.: Preparation and characterization of hexagonal W-type barium ferrite nanoparticles. Prog. Colloid & Polym. Sci. **135**, 38–43 (2008)
9. Kozakov, A.T., Kochur, A.G., Googlev, K.A., Nikolsky, A.V., Raevski, I.P., Smotrakov, V.G., Yeremkin, V.V.: X-ray photoelectron study of the valence state of iron in iron-containing single-crystal ($BiFeO_3$, $PbFe_{1/2}Nb_{1/2}O_3$), and ceramic ($BaFe_{1/2}Nb_{1/2}O_3$) multiferroics. J. Electron Spectrosc. Relat. Phenom. **184**, 16–23 (2011)
10. Bukhtiyarova, M.V., Ivanova, A.S., Slavinskaya, E.M., Plyasova, L.M., Rogov, V.A., Kaichev, V.V., Noskov, A.S.: Catalytic combustion of methane on substituted strontium ferrites. Fuel **90**, 1245–1256 (2011)
11. Shannon, R.D.: Revised effective ionic radii and systematic studies of interatomic distances in halides and chalcogenides. Acta Crystallogr. A, Found. Crystallogr. **32**, 751–767 (1976)
12. Cheng, F.X., Jia, J.T., Xu, Z.G., Zhou, B., Liao, C.S., Yan, C.H., Chen, L.Y., Zhao, H.B.: Microstructure, magnetic and magneto–optical properties of chemical synthesized Co–RE (RE = Ho, Er, Tm, Yb, Lu) ferrite nanocrystalline films. J. Appl. Phys. **86**, 2727–2732 (1999)
13. Pant, R.P., Arora, M., Kaur, B., Kumar, V., Kumar, A.: Finite size effect on Gd^{3+} doped $CoGd_xFe_{2-x}O_4$ ($0.0 \leq x \leq 0.5$) particles. J. Magn. Magn. Mater. **322**, 3688–3691 (2010)
14. Xu, J.J., Zou, H.F., Li, H.Y., Li, G.H., Gan, S.C., Hong, G.Y.: Influence of Nd^{3+} substitution on the microstructure and electromagnetic properties of barium W-type hexaferrite. J. Alloys Compd. **490**, 552–556 (2010)
15. Jotania, R.B., Khomane, R.B., Chauhan, C.C., Menon, S.K., Kulkarni, B.D.: Synthesis and magnetic properties of barium–calcium hexaferrite particles prepared by sol–gel and microemulsion techniques. J. Magn. Magn. Mater. **320**, 1095–1101 (2008)
16. Ahmed, M.A., Okasha, N., Kershi, R.M.: Influence of rare-earth ions on the structure and magnetic properties of barium W-type hexaferrite. J. Magn. Magn. Mater. **320**, 1146–1150 (2008)
17. Jacob, B.P., Thankachan, S., Xavier, S., Mohammed, E.M.: Dielectric behavior and AC conductivity of Tb^{3+} doped $Ni_{0.4}Zn_{0.6}Fe_2O_4$ nanoparticles. J. Alloys Compd. **541**, 29–35 (2012)
18. Bensebaa, F., Zavaliche, F., L'Ecuyer, P., Cochrane, R.W., Veres, T.: Microwave synthesis and characterization of Co-ferrite nanoparticles. J. Colloid Interface Sci. **277**, 104–110 (2004)
19. Epling, W.S., Hoflund, G.B., Weaver, J.F.: Surface characterization study of Au/α-Fe_2O_3 and Au/Co_3O_4 low-temperature CO oxidation catalysts. J. Phys. Chem. **100**, 9929–9934 (1996)
20. Jiang, K., Zhu, J.J., Wu, J.D., Sun, J., Hu, Z.G., Chu, J.H.: Influences of oxygen pressure on optical properties and interband electronic transitions in multiferroic bismuth ferrite nanocrystalline films grown by pulsed laser deposition. ACS Appl. Mater. Interfaces **3**, 4844–4852 (2011)
21. Gao, S.Y., Shi, Y.G., Zhang, S.X., Jiang, K., Yang, S.X., Li, Z.D., Takayama-Muromachi, E.: Biopolymer-assisted green synthesis of iron oxide nanoparticles and their magnetic properties. J. Phys. Chem. C **112**, 10398–10401 (2008)
22. Liu, X.S., Zhong, W., Yang, S., Yu, Z., Gu, B.X., Du, Y.W.: Influences of La^{3+} substitution on the structure and magnetic properties of M-type strontium ferrites. J. Magn. Magn. Mater. **238**, 207–214 (2002)

23. Ali, I., Islam, M.U., Ishaque, M., Khan, H.M., Ashiq, M.N., Rana, M.U.: Structural and magnetic properties of holmium substituted cobalt ferrites synthesized by chemical co-precipitation method. J. Magn. Magn. Mater. **324**, 3773–3777 (2012)
24. Rai, B.K., Mishra, S.R., Nguyen, V.V., Liu, J.P.: Synthesis and characterization of high coercivity rare-earth ion doped $Sr_{0.9}RE_{0.1}Fe_{10}Al_2O_{19}$ (RE: Y, La, Ce, Pr, Nd, Sm, and Gd). J. Alloys Compd. **550**, 198–203 (2013)
25. Fang, Q.Q., Bao, H., Fang, D., Wang, J.: Temperature dependence of magnetic properties of zinc and niobium doped strontium hexaferrite nanoparticles. J. Appl. Phys. **95**, 6360–6363 (2004)
26. Shirsath, S.E., Toksha, B.G., Jadhav, K.M.: Structural and magnetic properties of In^{3+} substituted $NiFe_2O_4$. Mater. Chem. Phys. **117**, 163–168 (2009)